NANO LETTERS

pubs.acs.org/NanoLett Letter

Intermolecular Stabilization Enables Long-Life, Low-Temperature-Resilient Amino-Anthraquinone Anodes for Sodium-Ion Batteries

Yuanyuan Quan, Wenwen Deng,* Qingqing Ma, Chunxian Guo,* and Zhong Jin*

Cite This: *Nano Lett.* 2026, 26, 1019−1026 Read Online

ACCESS | Metrics & More | Article Recommendations | Supporting Information

ABSTRACT: Organic electrode materials (OEMs) are promising for sodium-ion batteries but often suffer from dissolution and poor durability. We report a bis-anthraquinone anode, DABT, in which amino groups lower the redox potential and form hydrogen bonds to suppress dissolution. DABT delivers ∼245 mAh g^{-1} at an average voltage of ∼1.54 V, with an initial Coulombic efficiency of 98% and 79% capacity retention after 2500 cycles at 2C. Ex situ characterizations reveal a reversible C═O ↔ C−O conversion, coordinating Na^+ at four carbonyl sites. Paired with a $Na_3V_2(PO_4)_3$ cathode, the full cell achieves 160 mAh g^{-1} at 0.5C with an average voltage of ∼1.5 V, retaining >60% capacity after 500 cycles at 5C. Notably, the DABT//$Na_3V_2(PO_4)_3$ full cell retains 84% capacity at −20 °C after 100 cycles, underscoring robust low-temperature performance. This study provides a concise molecular-engineering strategy for high-performance organic anodes and advances the practical deployment of SIBs.

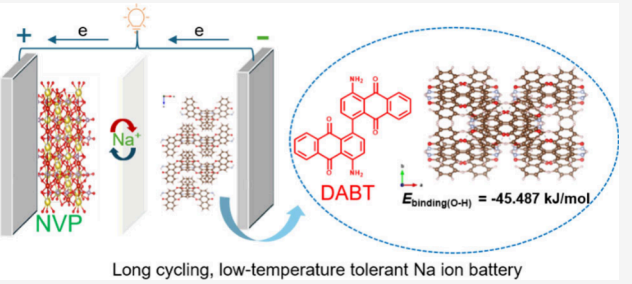

KEYWORDS: *sodium-ion batteries, organic electrode, bis-anthraquinone anode, intermolecular hydrogen bonds*

With the rapid expansion of renewables, scalable, low-cost, and sustainable energy storage has become urgent.[1−3] Sodium-ion batteries (SIBs) are attractive owing to Earth-abundant sodium, favorable economics, and intercalation chemistries analogous to Li systems.[4] Yet the larger Na^+ radius slows diffusion and accelerates structural degradation in conventional inorganic anodes, compromising cycle life and impeding deployment.[5] Organic electrode materials (OEMs) offer a compelling alternative: their compositions are resource-rich and environmentally benign,[6] and their electrochemistry can be precision-tuned through molecular design—backbone engineering, functional-group substitution, and polymerization—to optimize potential, kinetics, and stability. Lightweight frameworks with flexible redox centers enable fast Na^+ storage and multielectron transfer, delivering high specific capacities.[7] Coupled with inherent sustainability and recyclability, these attributes position OEMs as a promising direction for next-generation SIB anodes.[8]

Among various organic anode materials, sodium carboxylate salts are the most widely studied exemplars, e.g., disodium terephthalate (Na_2TP)[9] and sodium naphthalene dicarboxylates (Na_2−NDC),[10] whose redox relies on the reversible enolate conversion of $-COO^-$/C═O groups. Nevertheless, a low initial Coulombic efficiency arises from their intrinsically low redox potentials (<1.0 V vs Na^+/Na), which drive first-cycle electrolyte decomposition and irreversible SEI formation, consuming sodium and reducing capacity.[11] Although strategies such as presodiation, electrolyte/SEI engineering, polymerization, and conductive composites have improved performance, a complete solution remains elusive.[12] These limitations motivate the exploration of alternative organic anode motifs with elevated redox potentials, suppressed dissolution, and high ICE, enabled by rational molecular design and electrode/electrolyte engineering.

Anthraquinone (AQ) and derivatives have long been explored as cathode materials for SIBs due to well-defined carbonyl centers and rigid π-backbones.[13] AQ typically operates at ∼2.0 V vs Na^+/Na,[14] which is insufficient for high-energy cathodes. Crucially, AQ's redox potential is molecularly tunable: grafting electron-donating substituents (−OH, $-NH_2$) lowers the potential and shifts AQ into the anode window, with $-NH_2$ exerting a stronger donating effect than −OH.[15,16] This strategy opens a pathway to repurpose AQ frameworks as low-voltage anodes. Yet unmodified/small-molecule AQ systems still suffer from high solubility, low electronic conductivity, and loose packing, leading to low ICE, rapid fading, and poor rate performance.[17] Current advances are dominated by interfacial/electrolyte tactics—carbon coatings, high-concentration electrolytes, and solid-state electrolytes—whereas molecular-level redesign of anthraquinone

Received: October 27, 2025
Revised: January 9, 2026
Accepted: January 12, 2026
Published: January 15, 2026

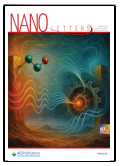

https://doi.org/10.1021/acs.nanolett.5c05364
Nano Lett. 2026, 26, 1019−1026

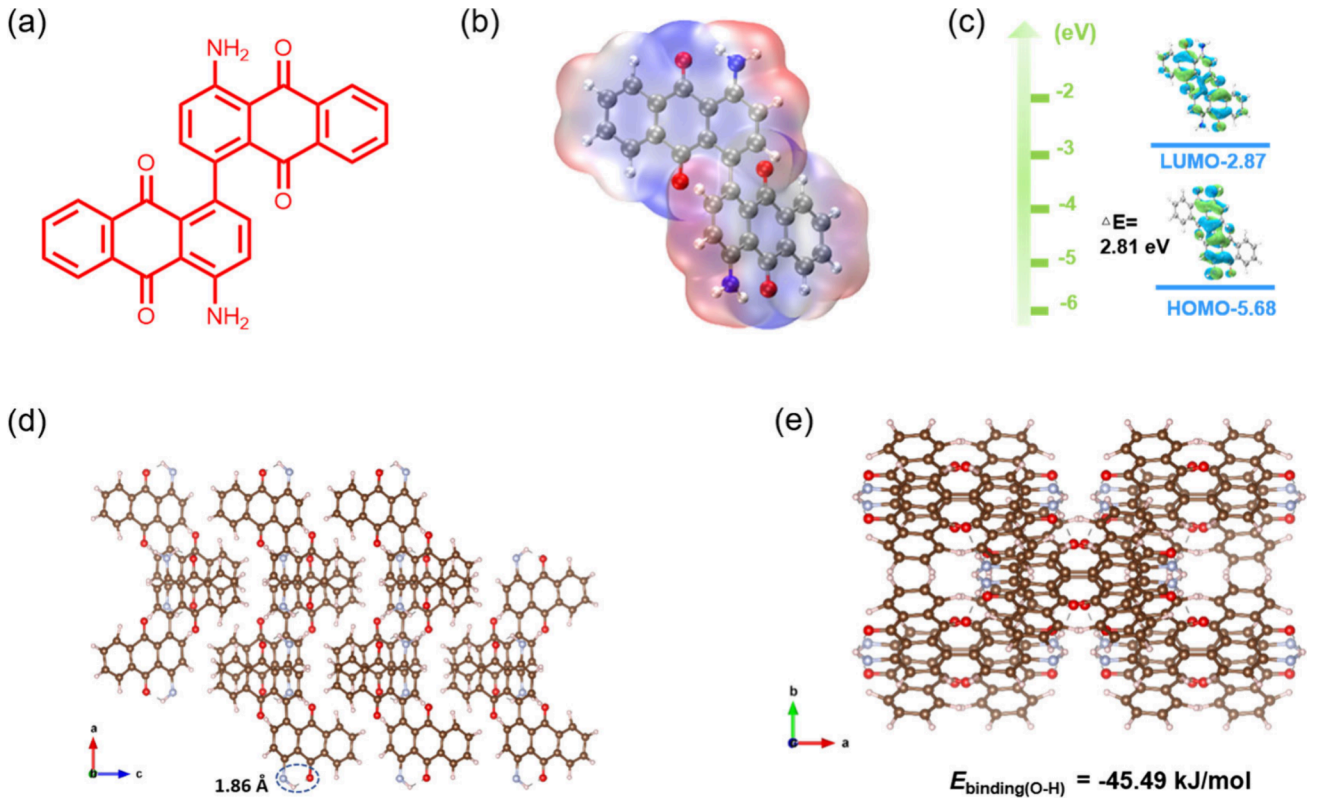

Figure 1. (a) Molecular structure of the DABT. (b) Electrostatic potential (ESP) surface highlighting the electron-rich carbonyl O atoms and electron-deficient N−H groups. (c) Frontier molecular orbital energy levels of DABT. (d) Crystal packing of DABT showing an intramolecular NH···O hydrogen bond with a bond length of 1.86 Å. (e) Intermolecular hydrogen-bonded network of DABT.

(AQ) to simultaneously depress redox potential and suppress dissolution remains underexplored.[18]

Here, guided by molecular design principles, we identify and validate a bis-anthraquinone anode, 4,4′-diamino-[1,1′-bianthracene]-9,9′,10,10′-tetrone (DABT), which addresses these limitations through a concise, molecule-centric strategy. DABT links two 1-aminoanthraquinone units via a C−C bond and integrates (i) electron-donating $-NH_2$ groups that lower redox potential and, via intermolecular hydrogen bonding, suppress dissolution; (ii) four carbonyl active sites enabling efficient multielectron/multi-ion storage; and (iii) an extended π-conjugated backbone that enhances charge delocalization and electronic transport. Benefiting from these features, DABT achieves a capacity of 245 mAh g^{-1} at 0.1 C with an average voltage of ∼1.54 V, along with 98% initial Coulombic efficiency and 79% capacity retention after 2500 cycles at 2C. Ex situ FTIR and XPS verify the reversible C═O/C−O conversion, while DFT calculations confirm Na^+ coordination at the four carbonyl sites. In $Na_3V_2(PO_4)_3$ full cells, the material demonstrates robust cycling stability and maintains a high capacity at −20 °C, confirming its practical potential. This work provides a molecular design blueprint for next-generation organic anodes and promotes sustainable development of sodium-ion batteries.

Figure 1a depicts DABT as two anthraquinone units linked by a C−C single bond with amino substituents at the 4/4′ positions. The molecular electrostatic potential (ESP) map (Figure 1b) shows pronounced negative potential localized on the carbonyl oxygens—identifying the C═O groups as the primary redox-active sites—whereas the amine hydrogens bear positive potential and act as hydrogen-bond donors. Frontier-orbital analysis (Figure 1c) yields HOMO = −5.68 eV and LUMO = −2.87 eV (ΔE = 2.81 eV), indicative of a relatively narrow gap that is conducive to charge transfer and a lower redox potential. Crystal packing (Figure 1d) reveals an N−H···O hydrogen-bond network with a short H···O contact of 1.86 Å. Consistently, the intermolecular O···H binding energy is −45.49 kJ mol^{-1} (Figure 1e), evidencing strong hydrogen-bonding interactions that stabilize the lattice and help suppress DABT dissolution in the electrolyte. Compared to AQ, the two amino groups in DABT enable it to construct a stable intermolecular hydrogen-bond network through the "anchoring effect" of its amino groups. It is also noteworthy that DABT possesses two amino groups, which provide more sites for intermolecular hydrogen bonding. Therefore, DABT can form a larger and denser hydrogen-bond network, further enhancing the structural stability of the material and reducing the interfacial charge-transfer resistance of the organic cathode. This facilitates ordered and rapid charge transport within the molecule, accelerates the kinetics of the electrochemical redox reactions, and thereby contributes to the long-cycle-life performance of the DABT cathode.

The molecular structure and morphological characteristics of DABT were systematically investigated using Fourier-transform infrared spectroscopy (FTIR), X-ray diffraction (XRD), ^{13}C nuclear magnetic resonance (NMR), and scanning electron microscopy (SEM). As shown in Figure S1a, FTIR spectra display characteristic absorption bands at 1600−1700 cm^{-1} (C═O stretching), 3200−3400 cm^{-1} (N−H stretching), and 1100−1200 cm^{-1} (C−N stretching), confirming the presence of amine and carbonyl groups. SEM images (Figure S1b) reveal irregular particles smaller than 30 μm. Solid-state

https://doi.org/10.1021/acs.nanolett.5c05364
Nano Lett. 2026, 26, 1019−1026

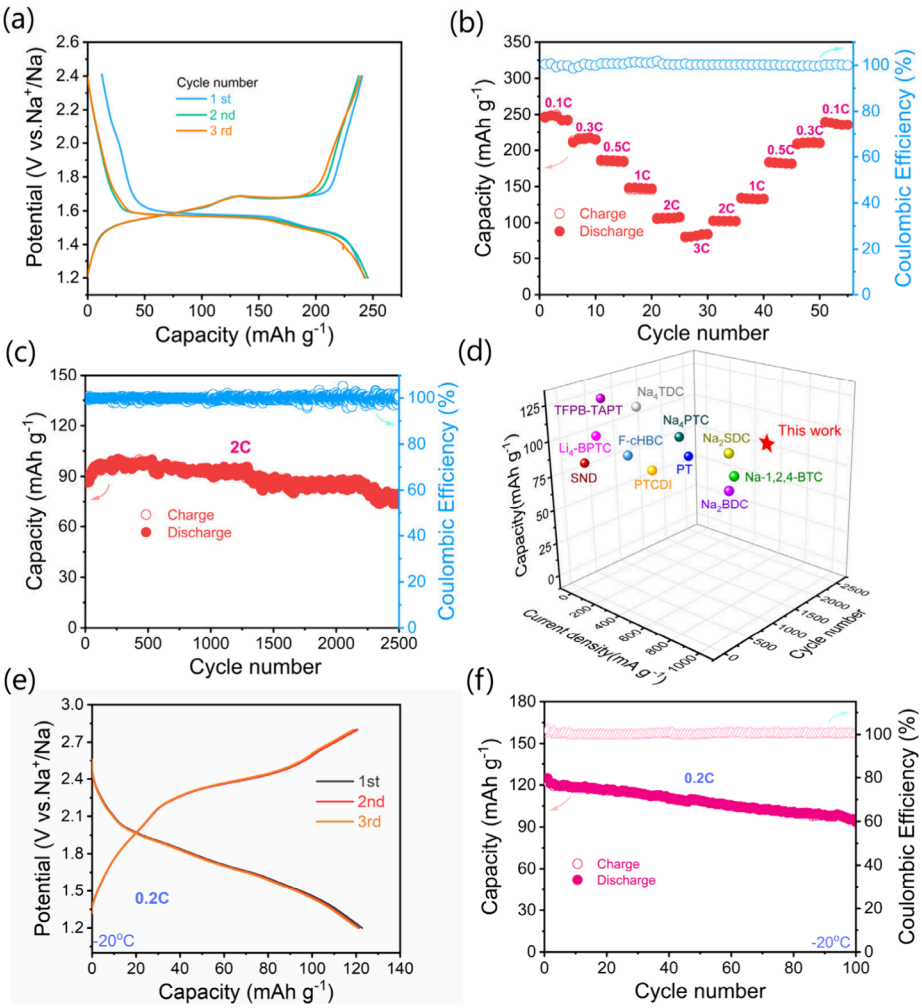

Figure 2. (a) Charge and discharge curves of DABT. (b) The rate performance of the DABT electrode. (c) The long-term cycle performance of the DABT electrode during 2500 cycles at 2C. (d) Comparison of DABT with related works. (e, f) The charge and discharge curves and cycling performance of DABT at −20 °C.

^{13}C NMR (Figure S1c) shows resonances at 180−188 ppm (carbonyl carbons) and 145−150 ppm (N-substituted aromatic carbons), with aromatic carbon signals at 100−140 ppm. XRD patterns (Figure S1d) exhibit sharp diffraction peaks, indicating high crystallinity. TGA results (Figure S2) demonstrate thermal stability up to 230 °C with a two-stage decomposition profile.

The galvanostatic charge−discharge (GCD) profiles in Figure 2a show first-cycle discharge/charge capacities of 241/243 mAh g^{-1}, corresponding to an initial Coulombic efficiency (CE) of 99%, markedly higher than that of most organic electrodes.[19] This high CE is primarily attributed to the moderate first-discharge potential (∼1.4−1.5 V vs Na/Na$^+$), which effectively suppresses low-potential-induced irreversible side reactions and excessive solid−electrolyte interphase (SEI) formation. Figure 2b assesses the rate performance under a stepwise sequence from 0.1C to 3C. As shown, the discharge capacity decreases from ∼245 mAh g^{-1} at 0.1C to ∼145 mAh g^{-1} at 1C and ∼95 mAh g^{-1} at 3C. When the current density returns to 0.1C, the capacity recovers to ∼235 mAh g^{-1} (≈96% of the initial value), underscoring robust structural integrity and rapid, highly reversible Na$^+$-storage kinetics. Figure 2c displays the long-term cycling performance of the DABT electrode at a current density of 2C. After 2500 cycles, the discharge capacity gradually decreases from ∼95 mAh g^{-1} to ∼75 mAh g^{-1}, corresponding to a capacity retention of approximately 80%. Figure 2d compares the performance of representative organic anode materials in a three-dimensional space defined by specific capacity, current density, and cycle life.[20−29] DABT sustains a reversible capacity of ∼100−110 mAh g^{-1} at a current density of 500 mA g^{-1} and retains 2500 cycles, evidencing synergistic optimization across the capacity−rate−lifetime space and highlighting its strong promise as an anode material for sodium-ion batteries. Organic cathodes suffer from intrinsic issues such as poor conductivity, dissolution, and limited cycle life, which are aggravated at low temperatures and cause fast capacity fade. To address this, we designed a hydrogen-bond-stabilized small molecule that improves electron conduction, structural stability, and dissolution resistance, thereby enhancing the low-temperature performance. As can be observed in Figure 2e, at −20 °C, the GCD profile of the Na//DABT battery remains well-defined, delivering a specific capacity of ≈125.5 mAh g^{-1}. Consistently, at the same temperature, the DABT cathode obtained ∼80% capacity retention after 100 cycles (Figure 2f), highlighting robust Na-storage kinetics under low-temperature conditions.

The electrochemical kinetics of the DABT-based electrode was evaluated using cyclic voltammetry (CV) measurements.

https://doi.org/10.1021/acs.nanolett.5c05364
Nano Lett. 2026, 26, 1019−1026

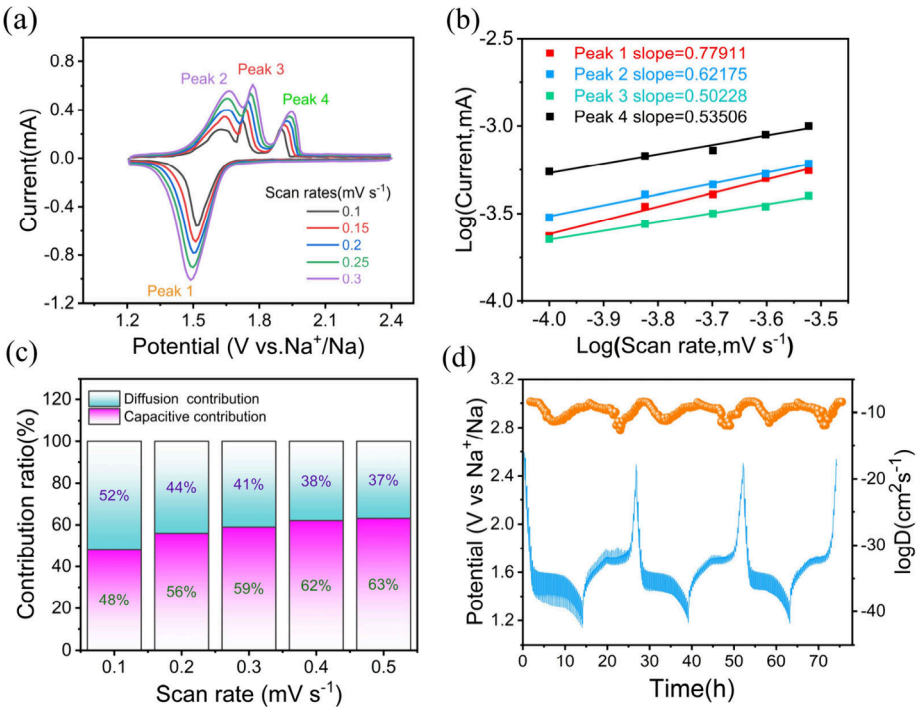

Figure 3. (a) CV curves at different scan rates. (b) Determination of *b*-values by plotting log(*i*) versus log(*v*) for Peaks 1−4. (c) Relative contributions of capacitive and diffusion-controlled processes at various scan rates. (d) GITT profiles illustrating the voltage response and corresponding diffusion coefficients during cycling.

As shown in Figure 3a, four distinct redox peaks (Peak 1−4) were observed, corresponding to multielectron transfer reactions. The peak current increased with scan rate, while the peak positions exhibited slight shifts, indicating typical quasi-reversible redox behavior. The *b*-values for Peaks 1−3 (Figure 3b) were obtained from the log *i*−log *v* plots using the following equation: log i = log a + b log v; here, i is the peak current (A) and v is the scan rate (mV s^{-1}). Linear fits yield b = 0.779, 0.621, and 0.502 for the three representative redox peaks. A slope of $b \approx 0.5$ indicates diffusion-controlled kinetics, whereas $b \approx 1.0$ reflects capacitive/surface-controlled behavior; intermediate values signify mixed contributions. To further quantify the capacitive contribution, the current response was deconvoluted according to $i(V) = k1v + k2v^{1/2}$.[30,31] As illustrated in Figure 3c, the capacitive contribution increased with scan rate, reaching 63% at 0.3 mV s^{-1}. This significant capacitive behavior is indicative of fast surface charge storage, which benefits the rate capability of the electrode. The sodium-ion diffusion kinetics were further evaluated by the galvanostatic intermittent titration technique (GITT). As shown in Figures 3d and S3, the GITT was performed by pulse charging/discharging with a constant current of 0.1C for 10 min (τ) followed by standing for 10 min to reach steady state voltage (E_s). The average sodium-ion diffusion coefficient (D) of DABT was calculated to be approximately10^{-10} cm^2 s^{-1}, which is comparable to or better than many reported organic cathode materials.[32−35] This favorable Na^+ diffusivity, combined with its capacitive-dominated kinetics, underpins the excellent electrochemical performance of the DABT electrode. Interestingly, the R_{ct} value of the DABT cathode decreased from 350 to around 100 Ω after 20 cycles and then stabilized at a lower value in subsequent cycles (Figure S4). This reduction and stabilization of R_{ct} promotes rapid interfacial charge conduction and reaction kinetics, thereby supporting the long-term cycling performance for the DABT cathode.

To gain further insights into the electrochemical redox mechanism of the DABT electrode, ex situ FTIR spectroscopy and ex situ high-resolution XPS analysis were performed at selected charge−discharge states in Figure 4a. As shown in Figure 4b, the FTIR spectra collected during the discharge and charge processes exhibit clear changes in characteristic vibrational bands. Specifically, the band at 1628 cm^{-1}, corresponding to the stretching vibration of C═O groups, gradually decreases in intensity as the battery discharges to 1.2 V (state d) and subsequently reappears upon charging to 2.4 V, indicating a reversible redox transformation of carbonyl groups. In parallel, changes in the C−N region (~1370 cm^{-1}) are also observed, suggesting local electronic environment fluctuations during redox cycling. High-resolution C 1s XPS spectra acquired at various electrochemical states further confirm these observations. As shown in Figure 4c, in the pristine state (a), typical deconvoluted peaks are assigned to C−C/C═C (284.8 eV), C−N (286.5 eV), and C═O (288.8 eV). Upon partial discharge to state b, a new peak at 287.3 eV emerges, corresponding to C−O groups, along with a simultaneous decrease in the C═O peak intensity. This indicates a partial reduction of carbonyl moieties to C−O single bonds. As the discharge progresses to state c (fully discharged), the C−O peak further intensifies, confirming the continuous reduction of carbonyl sites. When recharged to 2.4 V (state d), the C═O peak at 288.8 eV recovers significantly, suggesting that the redox-active carbonyl groups are reversibly involved in the charge storage process. Throughout the entire cycling process, the C═C/C−C and C−N signals remain largely unchanged, indicating the preservation of the conjugated backbone and molecular integrity. Notably, a small peak at 292.2 eV, attributed to C−

https://doi.org/10.1021/acs.nanolett.5c05364
Nano Lett. 2026, 26, 1019−1026

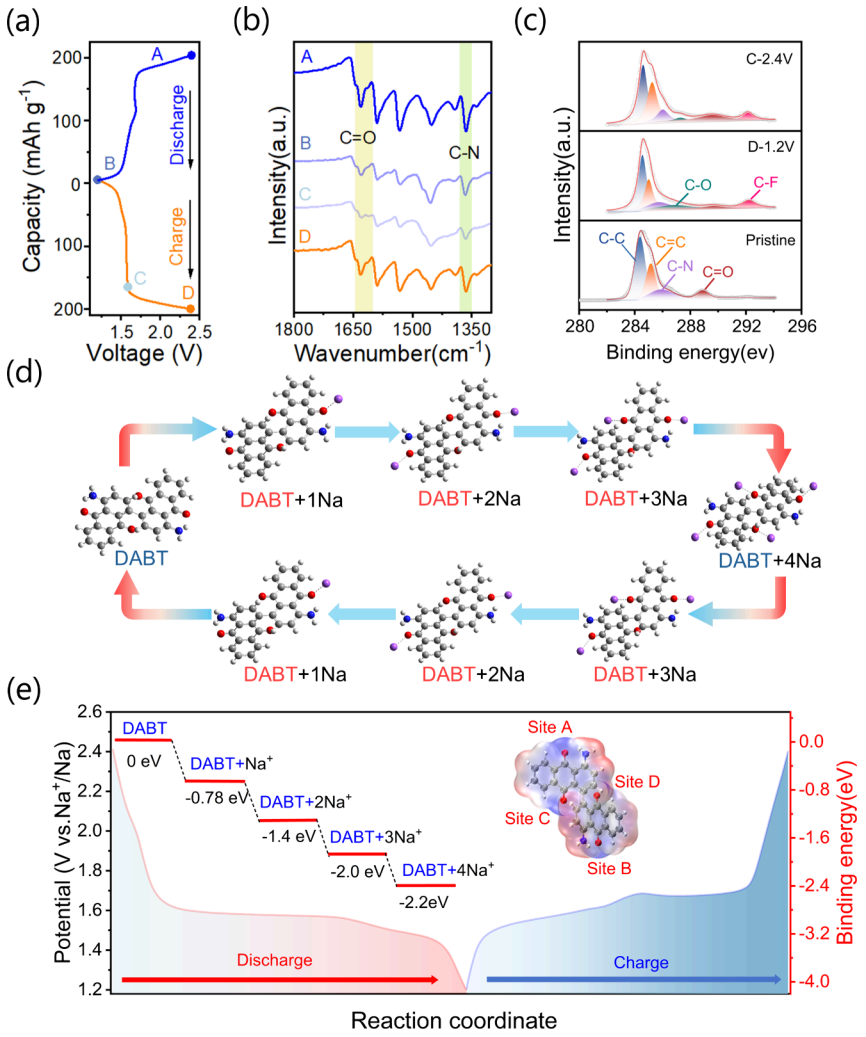

Figure 4. (a) Charge−discharge voltage−capacity profile of DABT during the first cycle at 0.3C; (b) in situ FTIR spectra of the DABT electrode at different states (labeled A, B, C, and D) during the first cycle; (c) ex situ XPS C 1s spectra of DABT in the pristine state, fully discharged state (D-1.2 V), and fully charged state (C-2.4 V) during the first cycle; (d) schematic illustration of the structural evolution of the DABT molecule during the stepwise reaction with sodium ions; (e) energy variation curve of DABT during sodium storage and the theoretical binding energies of sodium ions at different binding sites.

F bonds, is detected and is likely derived from electrolyte decomposition or polytetrafluoroethylene (PTFE). Ex situ SEM analysis was carried out to examine the morphology evolution of the DABT cathode during Na^+ insertion/extraction (Figure S5). As shown, the pristine DABT cathode exhibits an irregular block-like morphology with dispersed particles. Upon discharging to 1.2 V, particle aggregation becomes evident. When charged back to 2.4 V, the sample largely recovers its initial morphology,

Figure 4d schematically illustrates the proposed sodium-ion storage mechanism of the DABT molecule, which involves a four-step reversible enolization-like redox process. Each redox step corresponds to the coordination of one Na^+ ion to a carbonyl oxygen atom within the molecular structure. As the battery discharges, Na^+ ions sequentially insert into the DABT framework, forming C−O$^-$−Na^+ complexes, and reversibly deintercalate during the charging process. Corresponding structural evolution of DABT is shown in Scheme S1. Figure 4e presents the potential profile and binding energy landscape derived from Gaussian calculations. The calculated stepwise binding energies indicate a thermodynamically favorable Na^+ coordination at each stage of sodiation. Initially, a Na^+ ion preferentially coordinates with the carbonyl oxygen at Site A, forming DABT + 1Na, with a binding energy of −0.78 eV. Subsequently, a second Na^+ binds to the carbonyl at Site B, forming DABT + 2Na (−1.4 eV). As discharge proceeds, two more Na^+ ions insert into Sites C and D, forming DABT + 3Na and DABT + 4Na, with binding energies of −2.0 eV and −2.2 eV, respectively. The gradual decrease in binding energy with increasing Na^+ content supports a sequential, site-specific sodiation mechanism. As shown in Figure S6, the Gibbs free energies (ΔG) of intermediate states during the discharge−charge process were computed using this model. With progressive Na^+ insertion, the intermediate structures of Na_xDABT exhibit a gradual (monotonic) decrease in the ΔG, indicating increasingly stable Na-ion storage at the active sites. These thermodynamic trends validate the proposed Na-storage mechanism.

Practical applicability was evaluated by using a full sodium-ion cell comprising a DABT anode paired with a $Na_3V_2(PO_4)_3$ (NVP) cathode. Prior to pairing, the electrochemical performance of the Na//NVP half-cell was first assessed (Figure S7) to

https://doi.org/10.1021/acs.nanolett.5c05364
Nano Lett. 2026, 26, 1019−1026

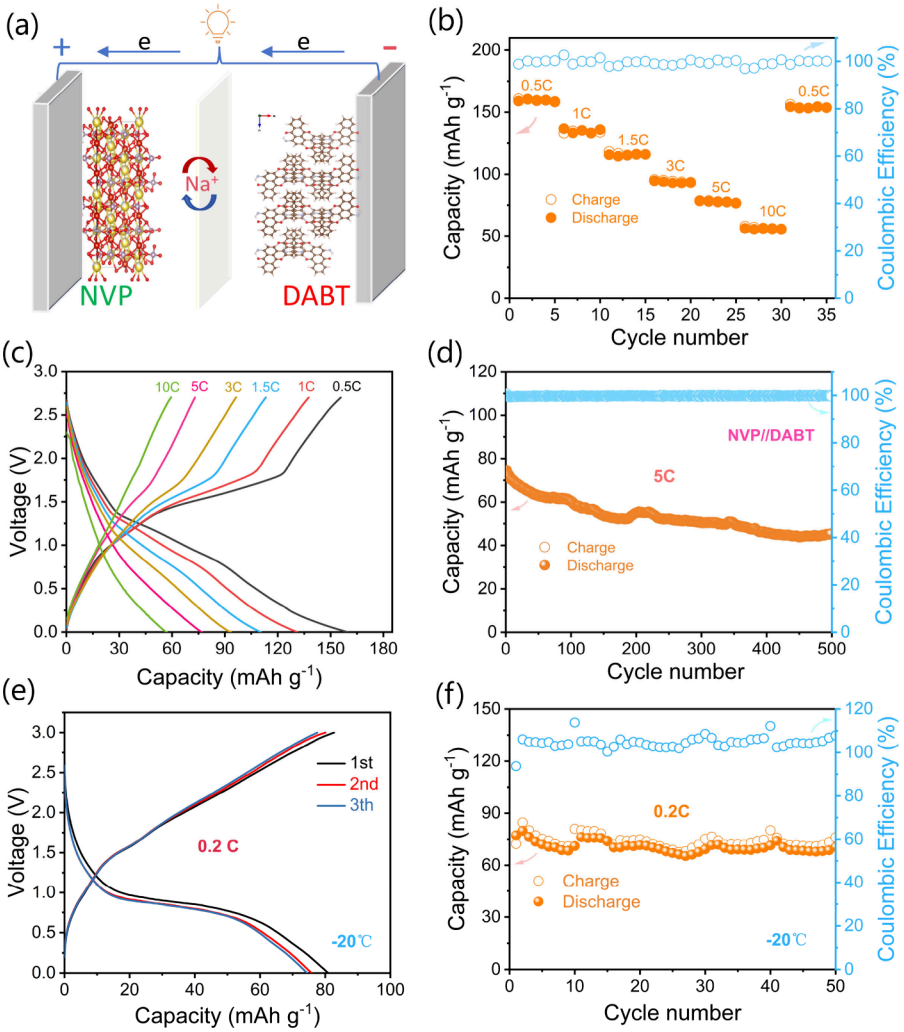

Figure 5. (a) Schematic illustration of the DABT//$Na_3V_2(PO_4)_3$ battery configuration. (b) Rate performance and Coulombic efficiency at various current rates (0.5−10C). (c) Charge−discharge profiles at different current rates. (d) Long-term cycling performance at a high rate of 5C. (e) Charge−discharge curves of the initial three cycles at a low temperature (−20 °C, 0.2C). (f) Cycling stability at −20 °C (0.2C).

ensure capacity matching and stability. Figure 5a illustrates the schematic configuration and working mechanism of the DABT//NVP full cell. As shown in Figure 5b, at 0.5C, the cell delivers a high discharge capacity of approximately 160 mAh g^{-1} (calculated based on the mass of the DABT anode), corresponding to the energy density of 62 Wh kg^{-1} (calculated based on the total mass of the cathode and anode). Even at higher rates of 3C and 5C, the cell maintains capacities of ∼90 mAh g^{-1} and ∼80 mAh g^{-1}, respectively. At 10C, the full cell delivers a capacity of 53 mAh g^{-1}. When the rate is returned to 0.5C, the capacity is recovered to 150 mAh g^{-1}, corresponding to 98% of its initial capacity, indicating robust structural stability and highly reversible electrochemical behavior. The galvanostatic charge−discharge (GCD) profiles of the full cell at various current rates (0.5−10 °C) are shown in Figure 5c, and it can be observed that the polarization slightly increases and the capacity decreases with increasing current density. Long-term cycling at 5C (Figure 5d) exhibits capacity retention over 60% after 500 cycles (73 to 46 mAh g^{-1}). As shown in Table S1, the integrated performance of the NVP//DABT battery is currently among the outstanding ones for the reported organic sodium-ion battery. Even at −20 °C and 0.2C (Figures 5e and 5f), the full cell achieves initial discharge capacities of ∼80 mAh g^{-1} with an average voltage of ∼1.25 V. After 50 cycles, capacity stabilizes at ∼75 mAh g^{-1} with 93% retention, showing high stability of the full cell at low temperature.

In this work, a novel carbonyl-rich organic anode material, DABT, was rationally designed for sodium-ion batteries. The DABT anode exhibits a high capacity of ∼245 mAh g^{-1} with an excellent rate and cycling performance from room temperature to −20 °C. Mechanistic analysis confirms a reversible four-electron redox process. Full cells deliver 160 mAh g^{-1} at 0.5C with >75% capacity retention after 250 cycles at 5C. Collectively, these results highlight the advantages of molecular-level redox design and confirm DABT's potential as a high-capacity, stable, and reversible organic anode for next-generation sodium-ion batteries.

■ ASSOCIATED CONTENT

Supporting Information

The Supporting Information is available free of charge at https://pubs.acs.org/doi/10.1021/acs.nanolett.5c05364.

Experimental details, structural characterization of DABT (Figure S1), thermogravimetric analysis (TGA) curves of DABT (Figure S2), the raw pulse curves of

https://doi.org/10.1021/acs.nanolett.5c05364
Nano Lett. 2026, 26, 1019−1026

DABT (Figure S3), EIS plots of DABT (Figure S4), SEM images of DABT electrodes under different conditions (Figure S5), schematic illustration of the structural evolution of DABT (Scheme S1), Gibbs free energy during the redox path of DABT (Figure S6), electrochemical performances of NVP (Figure S7), and the summary for all organic Na-ion batteries (Table 1) (PDF)

AUTHOR INFORMATION

Corresponding Authors

Wenwen Deng − *School of Material Science and Engineering, Suzhou University of Science and Technology, Suzhou 215000, China; School of Materials Science and Engineering, School of Chemistry and Chemical Engineering, Key Laboratory of Structure and Functional Regulation of Hybrid Materials of Ministry of Education, Anhui University, 230601 Hefei, P.R. China; State Key Laboratory of Coordination Chemistry, MOE Key Laboratory of Mesoscopic Chemistry, MOE Key Laboratory of High Performance Polymer Materials and Technology, Jiangsu Key Laboratory of Green Energy Catalysis and Intelligent Chemical Engineering, Suzhou Key Laboratory of Green Intelligent Manufacturing of New Energy Materials and Devices, Tianchang New Materials and Energy Technologies Research Center, Institute of Green Chemistry and Engineering, School of Chemistry and Chemical Engineering, Nanjing University, Nanjing, Jiangsu 210023, PR China*; Email: 24177@ahu.edu.cn

Chunxian Guo − *School of Material Science and Engineering, Suzhou University of Science and Technology, Suzhou 215000, China*; orcid.org/0000-0002-2603-7181; Email: cxguo@usts.edu.cn

Zhong Jin − *State Key Laboratory of Coordination Chemistry, MOE Key Laboratory of Mesoscopic Chemistry, MOE Key Laboratory of High Performance Polymer Materials and Technology, Jiangsu Key Laboratory of Green Energy Catalysis and Intelligent Chemical Engineering, Suzhou Key Laboratory of Green Intelligent Manufacturing of New Energy Materials and Devices, Tianchang New Materials and Energy Technologies Research Center, Institute of Green Chemistry and Engineering, School of Chemistry and Chemical Engineering, Nanjing University, Nanjing, Jiangsu 210023, PR China*; orcid.org/0000-0001-8860-8579; Email: zhongjin@nju.edu.cn

Authors

Yuanyuan Quan − *School of Material Science and Engineering, Suzhou University of Science and Technology, Suzhou 215000, China*; orcid.org/0009-0004-7378-1992

Qingqing Ma − *School of Materials Science and Engineering, School of Chemistry and Chemical Engineering, Key Laboratory of Structure and Functional Regulation of Hybrid Materials of Ministry of Education, Anhui University, 230601 Hefei, P.R. China*

Complete contact information is available at: https://pubs.acs.org/10.1021/acs.nanolett.5c05364

Notes

The authors declare no competing financial interest.

ACKNOWLEDGMENTS

This work was funded by The Natural Science Foundation of the Jiangsu Higher Education Institutions of China (23KJB150032, 24KJA15004), National Natural Science Foundation of China (U25A20628, 22561160129, 22479074, 22475096), the Equipment Pre-Research and Ministry of Education Joint Fund (8091B02052407), the Fundamental Research Program Key Project of Jiangsu Province (BK20253008), the Science and Technology Major Project of Jiangsu Province (BG2024013), the Scientific and Technological Achievements Transformation Special Fund of Jiangsu Province (BA2023037), the Academic Degree and Postgraduate Education Reforming Project of Jiangsu Province (JGKT24_C001), the Key Core Technology Open Competition Project of Suzhou City (SYG2024122), the Open Research Fund of Suzhou Laboratory (SZLAB-1308-2024-TS005), and the Chenzhou National Sustainable Development Agenda Innovation Demonstration Zone Provincial Special Project (2023sfq11).

REFERENCES

(1) Chu, S.; Majumdar, A. Opportunities and Challenges for a Sustainable Energy Future. *Nature* **2012**, *488* (7411), 294−303.

(2) Dunn, B.; Kamath, H.; Tarascon, J.-M. Electrical Energy Storage for the Grid: A Battery of Choices. *Science* **2011**, *334* (6058), 928−935.

(3) Larcher, D.; Tarascon, J.-M. Towards Greener and More Sustainable Batteries for Electrical Energy Storage. *Nature Chem.* **2015**, *7* (1), 19−29.

(4) Hwang, J.-Y.; Myung, S.-T.; Sun, Y.-K. Sodium-Ion Batteries: Present and Future. *Chem. Soc. Rev.* **2017**, *46* (12), 3529−3614.

(5) Xiao, S.; Li, X.; Li, T.; Xiang, Y.; Chen, J. S. Practical Strategies for Enhanced Performance of Anode Materials in Na^+ /K^+ -Ion Batteries. *J. Mater. Chem. A* **2021**, *9* (12), 7317−7335.

(6) Shi, R.; Jiao, S.; Yue, Q.; Gu, G.; Zhang, K.; Zhao, Y. Challenges and Advances of Organic Electrode Materials for Sustainable Secondary Batteries. *Exploration* **2022**, *2* (4), No. 20220066.

(7) Wang, Q.; O'Carroll, T.; Shi, F.; Huang, Y.; Chen, G.; Yang, X.; Nevar, A.; Dudko, N.; Tarasenko, N.; Xie, J.; Shi, L.; Wu, G.; Zhang, D. Designing Organic Material Electrodes for Lithium-Ion Batteries: Progress, Challenges, and Perspectives. *Electrochem. Energy Rev.* **2024**, *7* (1), 15.

(8) Wu, Y.; Ye, H.; Li, Y. Molecular Engineering of Organic Electrode Materials for Beyond Lithium-Ion Batteries. *Adv. Funct Materials* **2025**, *35* (28), No. 2424329.

(9) Desai, A. V.; Morris, R. E.; Armstrong, A. R. Advances in Organic Anode Materials for Na-/K-Ion Rechargeable Batteries. *ChemSusChem* **2020**, *13* (18), 4866−4884.

(10) Russo, R.; Rabuel, F.; Morcrette, M.; Davoisne, C.; Gachot, G.; Jamali, A.; Toussaint, G.; Stevens, P.; Becuwe, M. Disodium Naphthalene Dicarboxylate Based Negative Electrode Engineering for Organic-Inorganic Hybrid Sodium Batteries. *Sustainable Materials and Technologies* **2023**, *36*, No. e00639.

(11) Deng, J.; Luo, W.; Chou, S.; Liu, H.; Dou, S. Sodium-Ion Batteries: From Academic Research to Practical Commercialization. *Adv. Energy Mater.* **2018**, *8* (4), No. 1701428.

(12) He, H.; Sun, D.; Tang, Y.; Wang, H.; Shao, M. Understanding and Improving the Initial Coulombic Efficiency of High-Capacity Anode Materials for Practical Sodium Ion Batteries. *Energy Storage Materials* **2019**, *23*, 233−251.

(13) Werner, D.; Apaydin, D. H.; Portenkirchner, E. An Anthraquinone/Carbon Fiber Composite as Cathode Material for Rechargeable Sodium-Ion Batteries. *Batteries & Supercaps* **2018**, *1* (4), 160−168.

(14) Mu, L.; Lu, Y.; Wu, X.; Ding, Y.; Hu, Y.-S.; Li, H.; Chen, L.; Huang, X. Anthraquinone Derivative as High-Performance Anode

Material for Sodium-Ion Batteries Using Ether-Based Electrolytes. *Green Energy & Environment* **2018**, *3* (1), 63−70.
(15) Hasan, F.; Mahanta, V.; Abdelazeez, A. A. A. Quinones for Aqueous Organic Redox Flow Battery: A Prospective on Redox Potential, Solubility, and Stability. *Adv. Materials Inter* **2023**, *10* (24), No. 2300268.
(16) Werner, D.; Greussing, V.; Pattis, D.; Gallmetzer, J. M.; Schimanofsky, C.; Wielend, D.; Liebl, S.; Stüwe, T.; Ciganek, M.; Krajčovič, J.; Irimia-Vladu, M.; Hofer, T. S.; Portenkirchner, E. Towards the All Organic Na-Ion Battery, Using Naturally Occurring Amino- and Hydroxy Substituted Anthraquinones. *Electrochim. Acta* **2025**, *530*, No. 146346.
(17) Lu, Y.; Zhang, Q.; Li, L.; Niu, Z.; Chen, J. Design Strategies toward Enhancing the Performance of Organic Electrode Materials in Metal-Ion Batteries. *Chem.* **2018**, *4* (12), 2786−2813.
(18) Wang, H.; Liu, G.; Zhou, W.; Wang, Y.; Dong, X. High-Potential and Stable Organic Cathode for Rechargeable Batteries with Fast-Charging and Wide-Temperature Adaptability. *Angew. Chem. Int. Ed* **2025**, *64* (4), No. e202416874.
(19) Li, X.; Wang, Y.; Lv, L.; Zhu, G.; Qu, Q.; Zheng, H. Electroactive Organics as Promising Anode Materials for Rechargeable Lithium Ion and Sodium Ion Batteries. *Energy Mater.* **2022**, *2* (2), No. 200014.
(20) Wang, C.; Xu, Y.; Fang, Y.; Zhou, M.; Liang, L.; Singh, S.; Zhao, H.; Schober, A.; Lei, Y. Extended π-Conjugated System for Fast-Charge and -Discharge Sodium-Ion Batteries. *J. Am. Chem. Soc.* **2015**, *137*, 3124−3130.
(21) Medabalmi, V.; Wang, G.; Ramani, V. K.; Ramanujam, K. Lithium Salt of Biphenyl Tetracarboxylate as an Anode Material for Li/Na-Ion Batteries. *Appl. Surf. Sci.* **2017**, *418*, 9−16.
(22) Zhang, C.; He, Y.; Mu, P.; Wang, X.; He, Q.; Chen, Y.; Zeng, J.; Wang, F.; Xu, Y.; Jiang, J. Toward High Performance Thiophene-Containing Conjugated Microporous Polymer Anodes for Lithium-Ion Batteries through Structure Design. *Adv. Funct Materials* **2018**, *28* (4), No. 1705432.
(23) Wang, J.; Zhao, H.; Xu, L.; Yang, Y.; He, G.; Du, Y. Three-Electron Redox Enabled Dithiocarboxylate Electrode for Superior Lithium Storage Performance. *ACS Appl. Mater. Interfaces* **2018**, *10* (41), 35469−35476.
(24) Patra, B. C.; Das, S. K.; Ghosh, A.; Raj K, A.; Moitra, P.; Addicoat, M.; Mitra, S.; Bhaumik, A.; Bhattacharya, S.; Pradhan, A. Covalent Organic Framework Based Microspheres as an Anode Material for Rechargeable Sodium Batteries. *J. Mater. Chem. A* **2018**, *6* (34), 16655−16663.
(25) Park, J.; Lee, C. W.; Park, J. H.; Joo, S. H.; Kwak, S. K.; Ahn, S.; Kang, S. J. Capacitive Organic Anode Based on Fluorinated-Contorted Hexabenzocoronene: Applicable to Lithium-Ion and Sodium-Ion Storage Cells. *Advanced Science* **2018**, *5* (12), No. 1801365.
(26) Gu, T.; Gao, S.; Wang, J.; Cao, S.; Wang, K.; Zhou, M.; Jiang, K. Electrochemical Properties and Kinetics of Asymmetric Sodium Benzene-1,2,4-tricarboxylate as an Anode Material for Sodium-Organic Batteries. *ChemElectroChem.* **2020**, *7* (16), 3517−3521.
(27) Li, Z.; Zhang, Y.; Zhou, K.; Kong, T.; Zhou, X.; Hao, Y.; Huang, X.; Xu, J.; Cheng, Y.; Liu, H.; Guo, Z.; Wang, Y. A Safe Organic/Inorganic Composite Anode for Sodium-Ion Batteries. *Adv. Energy Mater.* **2024**, *14* (15), No. 2303786.
(28) Li, Z.; Wei, Y.; Zhou, K.; Huang, X.; Zhou, X.; Xu, J.; Kong, T.; Lucas Bao, J.; Dong, X.; Wang, Y. A Low Redox Potential and Long Life Organic Anode Material for Sodium-Ion Batteries. *Journal of Energy Chemistry* **2025**, *100*, 557−564.
(29) Dai, T.; Yang, B.; Wei, J.; Song, X.; Zhang, P.; Liu, Y.; Wen, S.; Li, H.; Yu, T.; Tie, Z.; Sun, H.; Yan, Y.; Jin, Z. Environmentally Benign and Long Cycling Mn-Ion Full Batteries Enabled by Hydrated Eutectic Electrolytes and Polycarbonyl Conjugated Organic Anodes. *J. Am. Chem. Soc.* **2025**, *147* (16), 13721−13731.
(30) Zheng, J.; Liu, X.; Li, W.; Li, W.; Feng, X.; Chen, W. Green Synthesis of Novel Conjugated Poly(Perylene Diimide) as Cathode with Stable Sodium Storage. *Nano Res.* **2023**, *16* (7), 9538−9545.
(31) Augustyn, V.; Simon, P.; Dunn, B. Pseudocapacitive Oxide Materials for High-Rate Electrochemical Energy Storage. *Energy Environ. Sci.* **2014**, *7* (5), 1597.
(32) Song, X.; Ge, Y.; Xue, X.; Ma, X.; Yu, Q.; Zhu, M.; Wang, Y.; Liang, J.; Tie, Z.; Ma, J.; Jin, Z. Electrolyte-Triggered in-Situ Polymerization of Multi-Site Organic Cathodes for Superior-Longevity Cation-Anion Co-Storage Secondary Batteries. *Chemical Engineering Journal* **2024**, *499*, No. 156359.
(33) Song, X.; Yu, Q.; Li, J.; Wu, Z.; Xing, Y.; Wang, Y.; Qin, L.; Sun, H.; Tie, Z.; Ma, J.; Jin, Z. In-Situ Electro-Polymerization of Aromatic Diimide Bridged N-Phenylcarbazole as High-Voltage Cathode Materials for Long-Lasting Cationic and Anionic Co-Storage Batteries. *Chemical Engineering Journal* **2025**, *512*, No. 162419.
(34) Jia, L.; Bao, P.; Fan, Z.; Liu, Y.; Yao, S.; Xu, Y. Oxime Organic Cathode Materials for Long-Lifespan Lithium-Ion Batteries. *J. Mater. Chem. A* **2025**, *13* (22), 16556−16564.
(35) Li, W.; Li, X.; Gu, Y.; Zhu, B.; Zheng, Y.; Shi, J.; Tang, W. Unveiling High-Voltage Organic Cathodes via Carbazole-Dihydrophenazine Conjugation for next-Generation Lithium Dual-Ion Batteries. *Mater. Today* **2025**, *88*, 229−239.

https://doi.org/10.1021/acs.nanolett.5c05364
Nano Lett. 2026, 26, 1019−1026